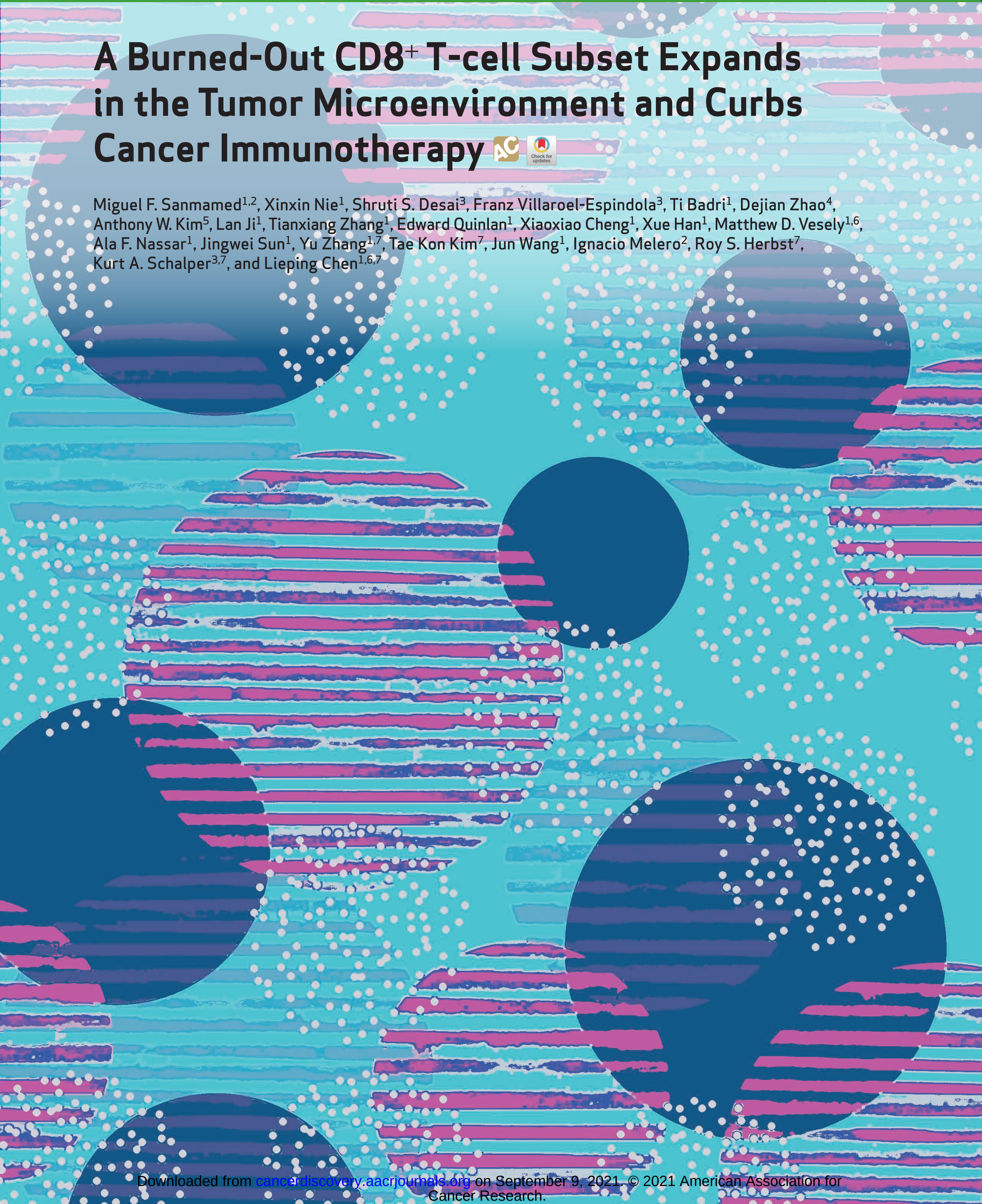

A Burned-Out CD8$^+$ T-cell Subset Expands in the Tumor Microenvironment and Curbs Cancer Immunotherapy

Miguel F. Sanmamed[1,2], Xinxin Nie[1], Shruti S. Desai[3], Franz Villaroel-Espindola[3], Ti Badri[1], Dejian Zhao[4], Anthony W. Kim[5], Lan Ji[1], Tianxiang Zhang[1], Edward Quinlan[1], Xiaoxiao Cheng[1], Xue Han[1], Matthew D. Vesely[1,6], Ala F. Nassar[1], Jingwei Sun[1], Yu Zhang[1,7], Tae Kon Kim[7], Jun Wang[1], Ignacio Melero[2], Roy S. Herbst[7], Kurt A. Schalper[3,7], and Lieping Chen[1,6,7]

ABSTRACT

Specific mechanisms by which tumor-infiltrating lymphocytes (TIL) become dysfunctional remain poorly understood. Here, we employed a two-pronged approach using single-cell mass cytometry and tissue imaging technologies to dissect TILs from 25 patients with resectable and 35 patients with advanced non–small cell lung cancer (NSCLC). We identified a burned-out CD8$^+$ TIL subset (Ebo) that specifically accumulated within the tumor microenvironment (TME) but not in adjacent nontumoral tissues. Ebo showed the highest expression of proliferation and activation markers but produced the lowest amount of IFNγ and were the most apoptotic CD8$^+$ TIL subset. Using a humanized patient-derived tumor xenograft model, we demonstrated that Ebo expansion occurred within the TME in a PD-1/B7-H1 pathway-dependent manner. Ebo abundance in baseline tumor tissues was associated with resistance to anti-PD therapy in patients with NSCLC. Our study identifies a dysfunctional TIL subset, with distinct features from previously described exhausted T cells, and implies strategies to overcome immunotherapy resistance.

SIGNIFICANCE: We identified a highly proliferative, overactivated, and apoptotic dysfunctional CD8$^+$ tumor-infiltrating subpopulation that is functionally distinct from previously described exhausted T cells. This population is expanded in lung cancer tissues in a PD-1/B7-H1-dependent manner, and its abundance is associated with resistance to cancer immunotherapy, thus becoming a potential tissue biomarker.

INTRODUCTION

Progressing tumors develop multiple cellular and molecular mechanisms to evade and/or resist immune attack. Collectively, these mechanisms are known as adaptive immune resistance. The archetype of these mechanisms is the upregulation of B7-H1 (PD-L1) in the tumor microenvironment (TME), which is primarily induced by IFNγ secretion from tumor-infiltrating lymphocytes (TIL; refs. 1, 2). These mechanisms typically result in the exclusion or functional impairment of TILs, thereby limiting endogenous antitumor immune response. Strategies such as blockade of the PD-1/B7-H1 pathway (hereafter referred to as anti-PD therapy) seek to correct and reinvigorate the impaired T-cell response against cancer (3), an approach described as normalization cancer immunotherapy (4). However, fundamental questions such as the specific mechanisms by which CD8$^+$ T cells become dysfunctional or how anti-PD therapy overcomes this dysfunctionality remain unanswered.

One major obstacle to understanding the mechanism of T-cell reinvigorating therapies is the cellular heterogeneity within the TME. Upon antigen presentation, T cells sequentially differentiate from naïve to effector and then to T memory cells in acute inflammatory conditions (5). However, in a chronic inflammatory environment such as the TME, CD8$^+$ T-cell differentiation could be altered or deviated, resulting in a greater diversity of subsets. Using chronic viral infection mouse models, a CD8$^+$ subtype referred to as exhausted T cells has been described (6). Exhausted CD8$^+$ T cells are characterized by the loss of IL2, TNFα, and IFNγ secretion; impaired proliferation; and high expression of coinhibitory receptors such as PD-1, LAG3, and TIM3 (7). A similar exhausted CD8$^+$ T-cell subset was subsequently identified within the TME of mouse tumors and patients with melanoma that was also characterized by high PD-1, LAG3, and TIM3 expression (8). However, recent studies indicate that patient CD8$^+$ TIL phenotype and functional profiles do not completely overlap with murine exhausted CD8$^+$ T cells observed in chronic infection models, and neither do the factors contributing to their differentiation (9, 10). The complex and unique ecosystem of the human TME that is composed of genetic tumor diversity, spatial heterogeneity, and asymmetric alteration by anticancer therapies likely contributes to CD8$^+$ TIL diversity and may determine unique pathways of CD8$^+$ TIL differentiation. In this regard, detailed characterization of dysfunctional human CD8$^+$ TILs and gaining a deeper understanding of the mechanisms leading to dysfunction

---

[1]Department of Immunobiology, Yale University, New Haven, Connecticut. [2]Division of Immunology and Immunotherapy, CIMA, Universidad de Navarra, Pamplona, Spain. [3]Department of Pathology, Yale University, New Haven, Connecticut. [4]Yale Center for Genome Analysis, Department of Genetics, Yale University, New Haven, Connecticut. [5]Division of Thoracic Surgery, Yale University, New Haven, Connecticut. [6]Department of Dermatology, Yale University, New Haven, Connecticut. [7]Department of Medicine (Medical Oncology), Yale University, New Haven, Connecticut.

Note: Supplementary data for this article are available at Cancer Discovery Online (http://cancerdiscovery.aacrjournals.org/).

M.F. Sanmamed, X. Nie, S.S. Desai, and F. Villaroel-Espindola contributed equally to this work. K.A. Schalper and L. Chen contributed equally to this work.

Corresponding Authors: Kurt A. Schalper, Yale University School of Medicine, 310 Cedar Street, New Haven, CT 06520. Phone: 203-988-5773; E-mail: kurt.schalper@yale.edu; and Lieping Chen, Yale University School of Medicine, 300 George Street, Suite 203A, New Haven, CT 06510. Phone: 203-373-1819; E-mail: lieping.chen@yale.edu

Cancer Discov 2021;11:1700–15

doi: 10.1158/2159-8290.CD-20-0962

are unmet needs that could be used to improve antitumor T-cell responses in patients.

Advances in high-resolution genomic and proteomic single-cell technologies allow for further dissection of the cellular diversity within TME, improving our ability to interrogate and characterize the patient's tumor–immune context. Specific advances in single-cell transcriptomics are a very powerful approach by which multiple aspects of cellular processes can be assessed (11, 12). Nevertheless, protein isoforms, post-translational modifications, proteolytic products, and cell-surface receptor/ligand protein expression are missed by this approach. In contrast, multiparametric proteomic single-cell analysis tools such as flow cytometry (13) and more recently cytometry by time of flight (CyTOF; ref. 14–16) or Imaging Mass Cytometry (IMC; ref. 17, 18), uniquely enable investigation of cell identity and behavior at the protein level, which are largely the key executors of biological processes. Clear understanding of the human immune TME has also been hampered by the lack of suitable experimental models. Patient-derived organoids (19, 20) and patient-derived explants (21) have been developed to recreate the complexity of the human immune TME. Although these models are increasingly utilized, they are limited by the short viability of immune cells (typically 2–3 days) and distinct drug pharmacodynamics and pharmacokinetics profiles when compared with *in vivo* settings. Alternatively, humanized patient-derived xenograft (PDX) models enriched with an autologous human immune system derived from peripheral blood mononuclear cells (PBMC; ref. 22), hematopoietic stem-progenitor cells ($CD34^+$; refs. 23, 24), or TILs (25, 26) have been proposed as an *in vivo* approach to recapitulate the tumor–immune cell interactions within the TME, offering longer experimental windows and more accurate pharmacokinetic/pharmacodynamic conditions.

In this study, we progressively dissected the $CD8^+$ TIL compartment in patients with non–small cell lung cancer (NSCLC), using a multilayered approach with orthogonal and complementary analysis platforms, including single-cell mass cytometry (CyTOF), quantitative immunofluorescence (QIF), IMC, and RNA sequencing (RNA-seq), to interrogate the nature and features of dysfunctional human T cells. Furthermore, to analyze the effect of PD-1/B7-H1 blockade on different human TIL subsets, we developed a humanized PDX model (herein referred to as immune PDX) in which intact patient-derived TILs can be experimentally modulated and analyzed. Our studies reveal a distinct dysfunctional $CD8^+$ TIL subset that expands within the TME in a PD-pathway–dependent manner. This $CD8^+$ TIL subset displays markers of end-stage differentiation, produces lower IFNγ upon stimulation, and shows increased apoptosis but is also highly proliferative. Finally, we demonstrate that this $CD8^+$ TIL subset accumulates in patients with more advanced NSCLC, and its higher abundance is associated with worse clinical response to anti-PD therapy.

RESULTS

Immune Profiling Reveals That CD8⁺ TILs Are Actively Expanding in NSCLC TME

Surgically resected tumoral (Tu) and nontumoral (non-Tu) paired lung tissues were obtained from 25 patients with resectable NSCLC. Specimens were divided into two mirroring halves and subjected to proteomic-based multiparametric CyTOF and QIF analysis (Supplementary Fig. S1A). We standardized a 39-plex CyTOF panel (Supplementary Table S1) including phenotypical and functional markers to interrogate lung tissue immune cell infiltration. Comparative analysis of T-cell abundance within the total non-Tu lung cell suspension by CyTOF or intact tissues by QIF showed a high correlation for both $CD8^+$ ($r = 0.74$, $P < 0.001$; Supplementary Fig. S1B) and $CD4^+$ ($r = 0.70$, $P = 0.0002$; Supplementary Fig. S1C) T-cell compartments, supporting the consistency of measurements and limited impact of our tissue digestion protocol. Rigorous validation of antibodies to recognize inducible markers was conducted using unstimulated versus stimulated human PBMCs (Supplementary Fig. S2). Next, we applied the aforementioned strategy to interrogate the immune composition of Tu and non-Tu lung tissues (Supplementary Fig. S1A). We defined the main immune cell populations based on the differential expression of specific-lineage markers (Fig. 1A; Supplementary Fig. S3A and S3B) and found that all lymphoid subsets were significantly increased in Tu tissues by CyTOF (Fig. 1A and B), and also by QIF (Fig. 1C) analysis. In contrast, non-lymphoid subsets were significantly less prominent in the TME, and the overall ratio of lymphoid cells to non-lymphoid cells was significantly higher in Tu tissues (Fig. 1D; Supplementary Fig. S4). Additionally, $CD8^+$ TILs were significantly more proliferative ($Ki\text{-}67^+$) than non-Tu $CD8^+$ T cells ($P < 0.0003$; Fig. 1E). Other lymphoid populations, including conventional $CD4^+$ T cells, T regulatory cells (Tregs), and B cells did not show a significant change in proliferation levels (Fig. 1E). These data indicate that $CD8^+$ TILs expand within the TME of patients with NSCLC and are the most proliferative TIL fraction.

A Proliferative, Terminally Differentiated CD8⁺ TIL Subset Selectively Expands in TME

To further understand why proliferative $CD8^+$ TILs are unable to control tumor growth in patients with NSCLC, we conducted a more comprehensive phenotypic and functional analysis of TILs by comparing them with lymphocytes from paired non-Tu lung tissues. Employing an unsupervised hierarchical clustering method named CITRUS (27), 2.1×10^4

Figure 1. Immune profiling reveals that $CD8^+$ TILs are actively expanding in NSCLC TME. Paired nontumoral (non-Tu) and tumoral (Tu) lung tissue from 25 surgically removed lobectomies was analyzed. **A,** Density *t*-SNE plots depicting the lymphoid and non-lymphoid subsets from pooled paired non-Tu (left) and Tu (right) lung tissues from patients with early clinical stage NSCLC. Results are shown for an equal number of pregated $CD45^+$ cells from both tissues. **B,** Frequency of lymphoid (top panel) and non-lymphoid (bottom panel) immune subsets across non-Tu and paired Tu tissues analyzed by CyTOF. **C,** Representative fluorescence microphotographs showing DAPI nuclear stain (blue) and each phenotypic marker: CD8, CD4, CD20, and CD68 (red) in paired non-Tu and Tu lung tissues studied by QIF. Dot plots depict QIF levels of CD8, CD4, CD20, and CD68 in non-Tu and Tu tissues. **D,** Ratio of $CD8^+$ T cells to $CD68^+$ cells from non-Tu and Tu paired lung tissues analyzed by QIF. **E,** KI-67 expression of CD8, CD4, Treg, and B cells from non-Tu and Tu paired lung tissues analyzed by CyTOF. *, $P < 0.05$; **, $P < 0.01$; ***, $P < 0.001$; ****, $P < 0.0001$. Mono, monocytes; Mac, macrophages; DC, dendritic cells; Neu, neutrophils; NK, natural killer.

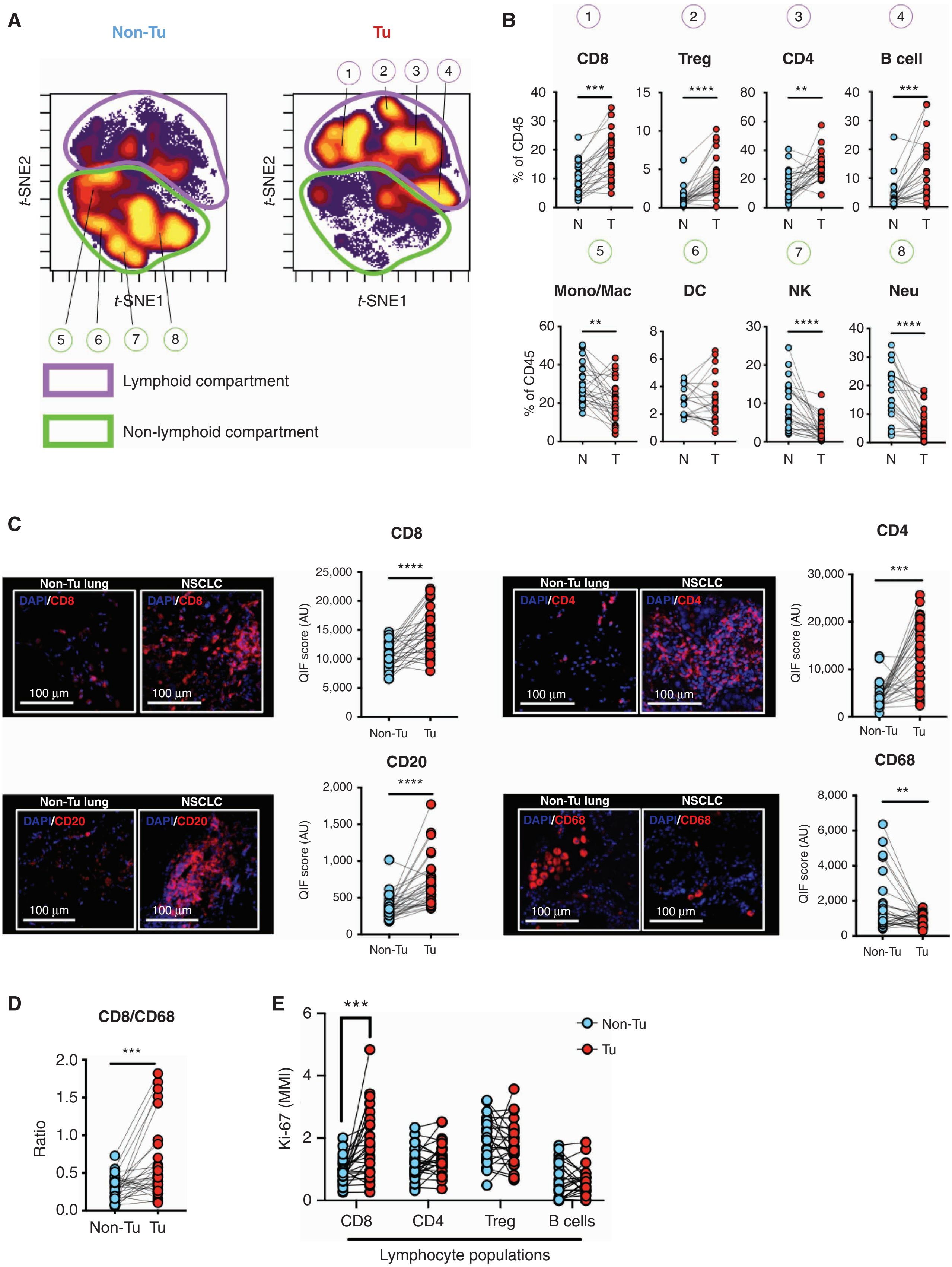
A
Non-Tu
Tu
t-SNE2
t-SNE1
1
2
3
4
5
6
7
8
Lymphoid compartment
Non-lymphoid compartment
B
CD8
Treg
CD4
B cell
Mono/Mac
DC
NK
Neu
% of CD45
N
T
***
****
**
C
Non-Tu lung
NSCLC
DAPI/CD8
DAPI/CD4
DAPI/CD20
DAPI/CD68
100 μm
CD8
CD4
CD20
CD68
QIF score (AU)
Non-Tu
Tu
D
CD8/CD68
Ratio
E
Ki-67 (MMI)
Non-Tu
Tu
CD8
CD4
Treg
B cells
Lymphocyte populations

CD3$^+$ T cells from Tu and non-Tu lung tissues were stratified according to the expression profile of phenotypic markers. In the first iteration, CITRUS automatically stratified tissue-infiltrating CD3$^+$ T cells in CD4$^+$ and CD8$^+$ branches (Fig. 2A; Supplementary Fig. S5A). Subsequently, CD8$^+$ T cells were segmented into two main populations of effector (Eff; CCR7$^-$CD45RA$^+$CD45RO$^-$) and effector memory (EM; CCR7$^-$CD45RA$^-$CD45RO$^+$) cells, showing that these two CD8$^+$ subgroups dominate the lung tissue infiltration (Fig. 2B and C; Supplementary Fig. S5B and S5C). The EM population was further subdivided into two additional subsets. One subset showed a conventional effector memory phenotype, referred to here as effector memory (Em) cells (Fig. 2B and C; Supplementary Fig. S5B and S5C). The other subset, in contrast, was characterized by high CD45RO, EOMES, FAS, CD27, CD28, KLRG1, PD-1, LAG3, and TIM3 expression. This profile is consistent with an activated, terminally differentiated, and proapoptotic phenotype, referred to here as burned-out effector (Ebo) cells (Fig. 2B–D; Supplementary Fig. S5B and S5C).

Comparison of functional markers across all three CD8$^+$ TIL subsets showed that Ebo cells had the highest levels of proliferation (Ki-67). In contrast, granzyme B (GzmB), TBET, and KLRG1 expression was more prominent in classic Eff cells. Interestingly, EOMES was highly expressed by both Ebo and Eff cells, but the ratio of EOMES to TBET was significantly higher in Ebo (median = 4.8) than Eff (median = 2.8) cells, consistent with an exhausted phenotype previously described in murine models, EOMES^{hi}TBET^{lo} (Fig. 2D; ref. 8). Additionally, these two effector CD8$^+$ T-cell populations were asymmetrically represented between TME and surrounding non-Tu lung tissues. While Ebo clusters were predominantly localized within the TME (false discovery rate [FDR] < 0.01; Fig. 2E), Eff clusters were more abundant in non-Tu lung tissues (FDR < 0.001; Fig. 2E). When we looked at PBMCs from patients with NSCLC, we observed that Ebo CD8$^+$ T cells were almost absent, similar to non-Tu lung tissues (Supplementary Fig. S5D). Paired Tu and non-Tu analysis revealed that Eff CD8$^+$ TILs express less GzmB and KLRG1 when compared with the paired non-Tu subsets, indicating a loss of function in addition to loss of cell numbers of Eff CD8$^+$ T cells within the TME (Fig. 2F). Finally, although expression of PD-1 and TIM3 was significantly increased in the three CD8$^+$ TIL subsets compared with non-Tu tissues, LAG3 expression was exclusively increased in Ebo, indicating that the LAG3 increase is a distinctive molecular feature of this subset (Fig. 2F). When we further stratified Ebo CD8 TIL cluster in high versus low Ki-67 expression, we observed that the high Ki-67 subpopulation displayed higher PD-1, LAG3, TIM3, and FAS expression levels (Supplementary Fig. S6A), and this subcluster appeared separately stratified in a *t*-distributed stochastic neighbor embedding (*t*-SNE) analysis (Supplementary Fig. S6B). These data reveal the existence of three major phenotypically distinct CD8$^+$ TIL subsets, among which Ebo stands out, as it is highly proliferative (Ki-67$^+$, CD28$^+$), fully activated (PD-1$^+$, LAG3$^+$, TIM3$^+$), terminally differentiated (EOMES^{hi}TBET^{lo}), and selectively expanded in the TME.

Ebo CD8$^+$ TILs Are a Transcriptionally Distinct and Dysfunctional Subset

Given that Ebo was the only subset selectively expanded in the TME, we further explored the transcriptional and functional characteristics of these cells in order to understand what was unique about them. TILs were isolated from freshly resected NSCLC specimens; the three CD8$^+$ TIL subsets were sorted by flow cytometry and processed for whole transcriptome RNA-seq analysis. Ebo showed greater transcriptional similarities with Em than with Eff CD8$^+$ TILs, consistent with our proteomic CITRUS clustering results (Supplementary Fig. S7A). Nevertheless, when we compared Ebo directly with the Em CD8$^+$ TIL population, we found a clearly distinct gene signature. Specifically, a total of 888 genes were significantly upregulated in Ebo over Em, and 881 genes were upregulated in Em over Ebo (FDR < 1%; adjusted $P < 0.01$), confirming that, although they are clustered together, these two cell populations are transcriptionally different (Fig. 3A). Consistent with our proteomic-based CyTOF analysis, Ki-67 gene expression was upregulated in Ebo compared with Em (Fig. 3B). Additionally, Ebo had higher expression of other transcripts associated with cell proliferation such as *POLR3K* and *DNA2*. In contrast, Em showed upregulated expression of genes related to tissue development and cellular differentiation, including *ARMCX2* and *FLIP1L* (Fig. 3A and B). In line with these data, gene set enrichment analysis (GSEA) showed proliferative signatures enriched in the Ebo population (Fig. 3C and D, left panel), whereas the Em population showed an enrichment for stem cell–type signatures (Fig. 3C and D, right panel). Furthermore, we analyzed T-cell receptor (TCR) sequencing transcripts from the three subsets and observed that Eff CD8$^+$ TILs displayed the highest clonality, whereas Ebo and Em showed a higher clonotype diversity (Fig. 3E and F; Supplementary Fig. S7B and S7C). No significant differential expression of the associated exhaustion markers *ENTPD1*, *TOX*, *NR4A2*, or *CD38* was found across the three subsets (Supplementary Fig. S7D). Next, we interrogated the functional capacity of these three CD8$^+$ TIL subsets to produce IFNγ. CD8$^+$ TIL subsets

Figure 2. Identification of three phenotypically distinct CD8$^+$ TIL subsets in patients with NSCLC. CD3$^+$ T cells ($n = 20{,}824$) from paired non-Tu ($n = 20$) and NSCLC ($n = 20$) specimens were analyzed using CITRUS. **A,** Visual representation of unsupervised hierarchical clustering. CD4 and CD8 compartments are contoured on the basis of canonical lineage markers as indicated in Supplementary Fig. S5. The color scale indicates the median mass intensity of CD8 expression, and node sizes are scaled on the basis of frequency of cells in each cluster. **B,** CD8$^+$ T-cell clusters are depicted. The three different subsets are contoured based on differential expression of markers: CCR7$^-$CD45RA$^+$CD45RO$^-$ (yellow), CCR7$^-$CD45RA$^-$CD45RO^{lo} (pink), and CCR7$^-$CD45RA$^-$CD45RO^{hi} (blue). The color scale indicates the median mass intensity of CD45RO expression. Node sizes are scaled on the basis of the frequency of cells in each cluster. **C,** Box plots depict expression levels of CD45RO (left), CD45RA (middle), and CCR7 (right) within each CD8 cluster identified as effector (Eff), effector memory (Em), and effector burned-out (Ebo). **D,** Heat map showing relative normalized expression of depicted markers in Eff, Em, and Ebo. Panels depict the expression levels of indicated markers in Eff, Em, and Ebo CD8$^+$ TIL subsets. **E,** The Significance Analysis of Microarrays (SAM) model described the clusters with significantly different abundance (FDR < 0.01) between nontumoral and tumoral lung tissue. **F,** Dot plots depict the marker intensity of each CD8 branch cluster from non-Tu and paired Tu lung tissue. *, $P < 0.05$; **, $P < 0.01$; ***, $P < 0.001$; ****, $P < 0.0001$.

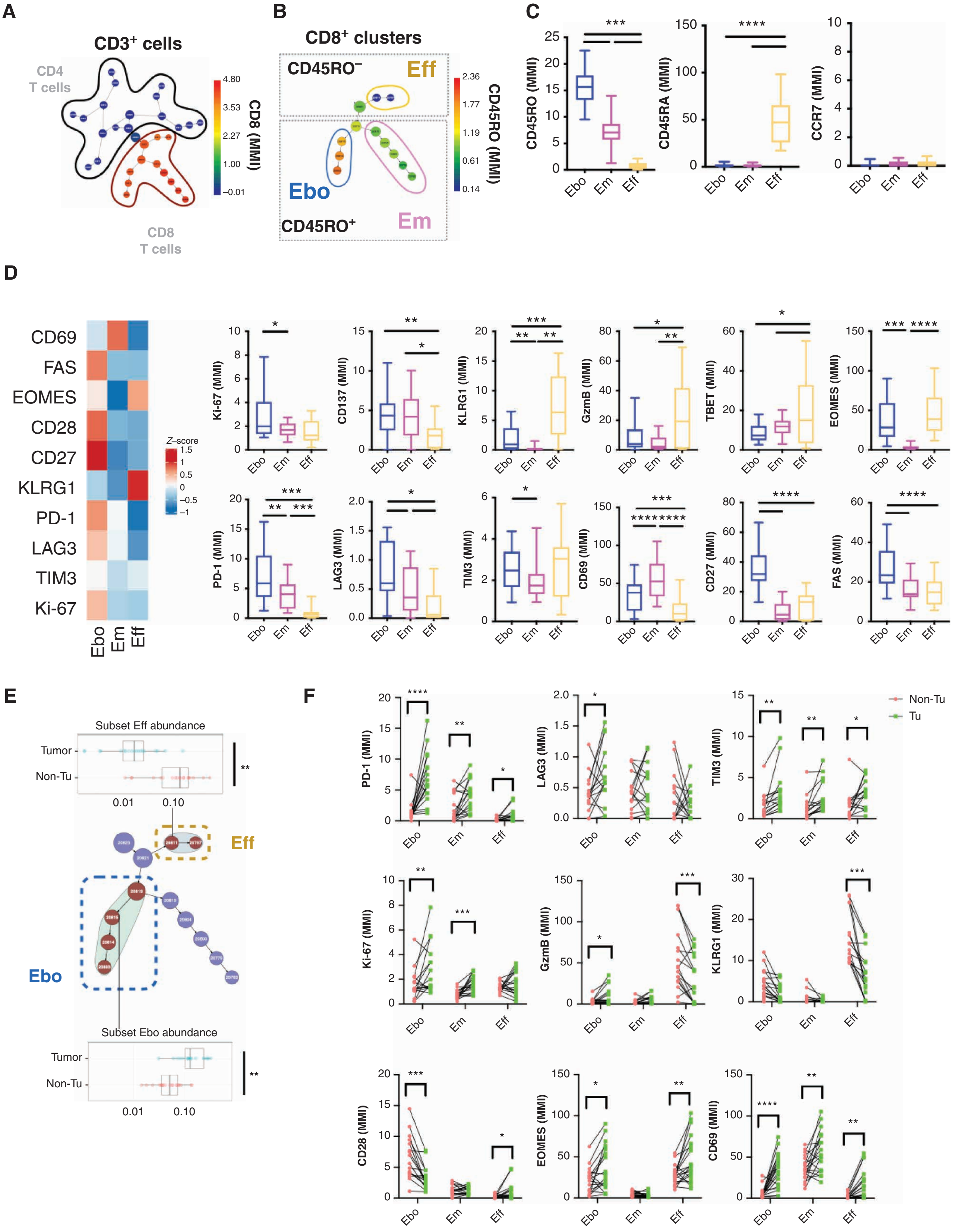
A
CD3+ cells
CD4 T cells
CD8 T cells
CD8 (MMI)
4.80
3.53
2.27
1.00
−0.01
B
CD8+ clusters
CD45RO−
Eff
CD45RO+
Ebo
Em
CD45RO (MMI)
2.36
1.77
1.19
0.61
0.14
C
CD45RO (MMI)
CD45RA (MMI)
CCR7 (MMI)
Ebo Em Eff
***
****
D
CD69
FAS
EOMES
CD28
CD27
KLRG1
PD-1
LAG3
TIM3
Ki-67
Ebo Em Eff
Z-score
1.5
1
0.5
0
−0.5
−1
Ki-67 (MMI)
CD137 (MMI)
KLRG1 (MMI)
GzmB (MMI)
TBET (MMI)
EOMES (MMI)
PD-1 (MMI)
LAG3 (MMI)
TIM3 (MMI)
CD69 (MMI)
CD27 (MMI)
FAS (MMI)
E
Subset Eff abundance
Tumor
Non-Tu
0.01
0.10
**
Eff
Ebo
Subset Ebo abundance
Tumor
Non-Tu
0.01
0.10
**
F
Non-Tu
Tu
PD-1 (MMI)
LAG3 (MMI)
TIM3 (MMI)
Ki-67 (MMI)
GzmB (MMI)
KLRG1 (MMI)
CD28 (MMI)
EOMES (MMI)
CD69 (MMI)
Ebo Em Eff

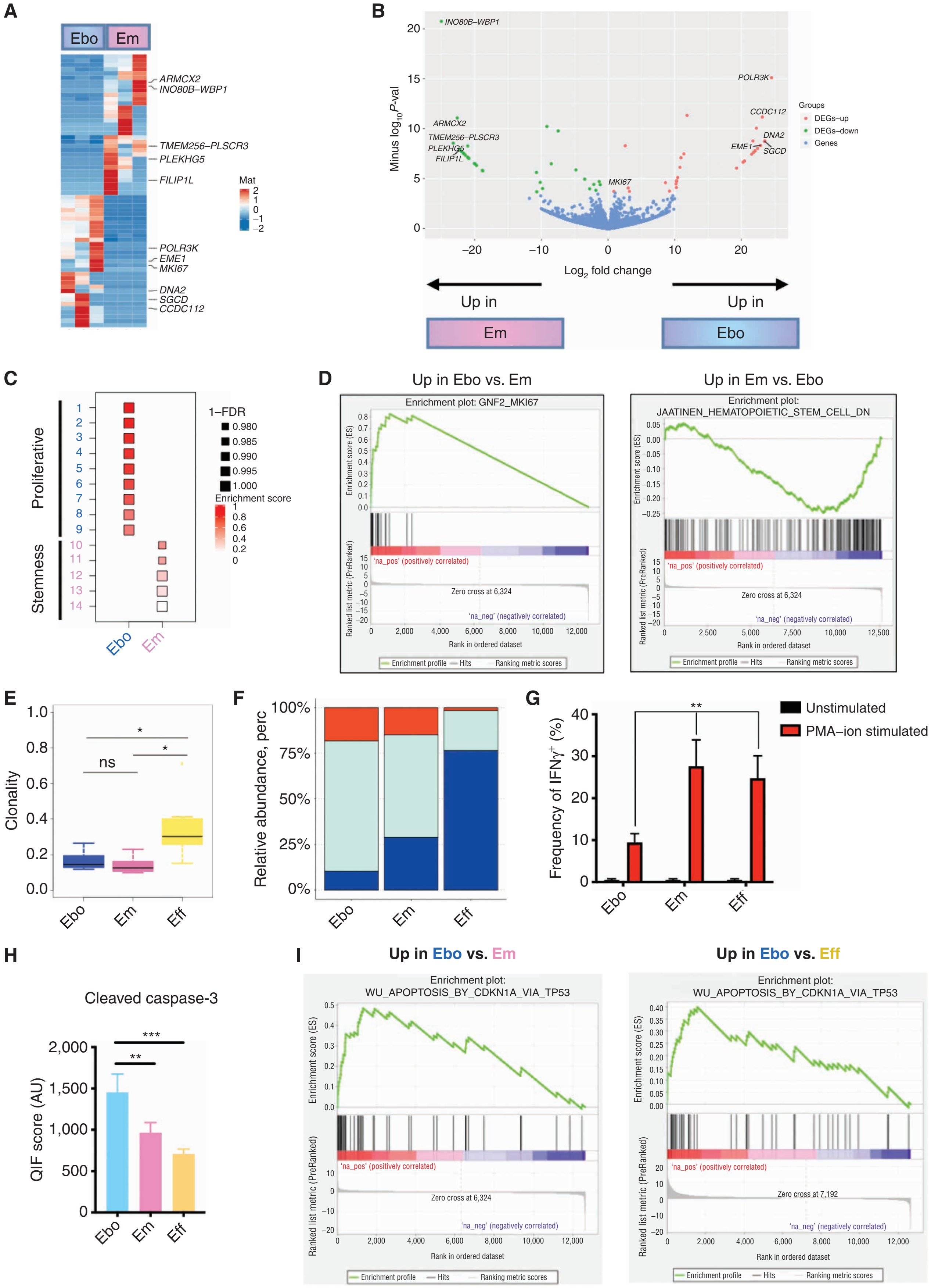
A
Ebo
Em
ARMCX2
INO80B–WBP1
TMEM256–PLSCR3
PLEKHG5
FILIP1L
POLR3K
EME1
MKI67
DNA2
SGCD
CCDC112
Mat
2
1
0
−1
−2
B
INO80B–WBP1
POLR3K
CCDC112
DNA2
EME1
SGCD
ARMCX2
TMEM256–PLSCR3
PLEKHG5
FILIP1L
MKI67
Minus $\log_{10}$ P-val
Log₂ fold change
Groups
DEGs–up
DEGs–down
Genes
Up in
Em
Up in
Ebo
C
Proliferative
Stemness
1–FDR
0.980
0.985
0.990
0.995
1.000
Enrichment score
1
0.8
0.6
0.4
0.2
0
Ebo
Em
D
Up in Ebo vs. Em
Enrichment plot: GNF2_MKI67
Up in Em vs. Ebo
Enrichment plot: JAATINEN_HEMATOPOIETIC_STEM_CELL_DN
Enrichment score (ES)
Ranked list metric (PreRanked)
'na_pos' (positively correlated)
Zero cross at 6,324
'na_neg' (negatively correlated)
Rank in ordered dataset
Enrichment profile
Hits
Ranking metric scores
E
Clonality
ns
*
*
Ebo
Em
Eff
F
Relative abundance, perc
100%
75%
50%
25%
0%
Ebo
Em
Eff
G
Frequency of IFNγ⁺ (%)
**
Unstimulated
PMA–ion stimulated
Ebo
Em
Eff
H
Cleaved caspase-3
QIF score (AU)
***
**
Ebo
Em
Eff
I
Up in Ebo vs. Em
Up in Ebo vs. Eff
Enrichment plot: WU_APOPTOSIS_BY_CDKN1A_VIA_TP53
Enrichment score (ES)
Ranked list metric (PreRanked)
'na_pos' (positively correlated)
Zero cross at 6,324
Zero cross at 7,192
'na_neg' (negatively correlated)
Rank in ordered dataset
Enrichment profile
Hits
Ranking metric scores

were sorted by flow cytometry from nine primary NSCLC tissues, and intracellular IFNγ expression was analyzed upon *ex vivo* PMA–ionomycin stimulation. Intriguingly, although Ebo cells showed the highest baseline expression of proliferation and activation markers, they produced the least amount of IFNγ when compared with the Em and Eff populations (Fig. 3G). Because Ebo showed the highest expression of FAS, a proapoptotic marker, we hypothesized that the lack of IFNγ production may be explained because these cells are engaged in cell death programs. To avoid induction of cleaved caspases that may occur during tissue digestion to harvest TILs, we optimized the use of QIF to measure cleaved caspases within intact tumor tissues (Supplementary Fig. S8A and S8B). Among the three $CD8^+$ TIL subsets, Ebo displayed the highest levels of cleaved caspase-3 expression as compared with the Em and Eff subsets (Fig. 3H; Supplementary Fig. S8C). Additionally, GSEA showed an apoptotic signature enriched in the Ebo subset. This signature is associated with cyclin-dependent kinase inhibitor 1A, which is considered instrumental in the execution of apoptosis following caspase activation (Fig. 3I). Together, these data show that the three $CD8^+$ TIL subsets are transcriptionally distinct, consistent with the clustering observed in CyTOF analysis, and indicate that the Ebo subset is enriched in apoptotic and dysfunctional $CD8^+$ T cells.

The B7-H1/PD-1 Pathway Mediates Ebo $CD8^+$ TIL Expansion within TME

To explore the dynamic changes of $CD8^+$ TIL subsets within the TME and their response to immunotherapy, we developed an immune-proficient PDX model. This alternative PDX model (immune-PDX), uses 4 to 5 mm^3 fresh primary NSCLC surgical specimens engrafted subcutaneously into NOD/SCID IL2R$\gamma^{-/-}$ (NSG) mice. Xenografts contain all human components of the patient's unique TME, including hematopoietic, stromal, and tumor cells, and support their modulation and study (Fig. 4A). We observed that $CD8^+$, $CD4^+$, B, natural killer T, and myeloid mononuclear phagocyte cellular composition remained constant for at least 2 weeks after engraftment (Fig. 4B and C). In contrast, natural killer cells and granulocytes significantly declined during the same period of time (Fig. 4B and C). We monitored the abundance of the three $CD8^+$ TIL subsets within the TME at baseline and 2 weeks after engraftment by CyTOF and found that Ebo significantly increased (27.6 ± 5.6%; $P = 0.0012$), but Em (−22.8 ± 4.6%; $P = 0.0010$) and Eff (−5.62 ± 2.75%; $P = 0.0755$) $CD8^+$ TILs progressively decreased over time (Fig. 4D and E). Interestingly, tumors expressing high B7-H1 levels maintained their expression for 2 weeks after engraftment (Supplementary Fig. S9), indicating that this pathway remains intact in this model and is amenable to modulation. To test the effect of anti-PD therapy on $CD8^+$ TIL populations, we treated immune-PDX engrafted with $B7\text{-}H1^+$ tumors with avelumab (anti-human B7-H1 mAb) or isotype control. $CD8^+$ TIL subsets were evaluated by CyTOF after two doses of treatment. As shown in Fig. 4F and G, avelumab treatment reduced the expansion of Ebo (−13.96 ± 4.44%; $P = 0.012$) and prevented the reduction of Eff (+3.978 ± 1.58%; $P = 0.0311$), resulting in a favorable Eff/Ebo ratio in avelumab-treated mice (Fig. 4F and G). Additionally, avelumab decreased the expression of the proapoptotic marker (BIM) in the Eff cells and increased the levels of the activation markers CD27 and CD69. These results suggest that B7-H1/PD-1 blockade may play a protective role for this population during activation (Fig. 4H). In both Eff and Em, TBET was significantly increased after B7-H1 blockade (Fig. 4H), in line with the observed *ex vivo* increased IFNγ production upon restimulation (Fig. 3E). These data demonstrate that the Ebo $CD8^+$ TIL subset is expanded within the TME over time and that this expansion can be reduced by B7-H1 blockade.

Ebo Abundance Is Associated with Tumor Progression and Resistance to Anti-PD Therapy

Because we observed that Ebo expands within human TME over time, we speculated that expansion of this dysfunctional $CD8^+$ T-cell population may correlate with advancing disease and contribute to immune escape and/or resistance to immunotherapy. To test this hypothesis, we standardized a 37-plex IMC panel (Supplementary Table S2) to identify the Ebo $CD8^+$ TIL subset in 35 patients with early and advanced NSCLC (Fig. 5A). Patients with NSCLC with clinical stage IV disease showed a significantly higher abundance of Ebo $CD8^+$ TILs than patients with clinical stage I disease (23.03 ± 7.42%; $P = 0.006$), supporting the notion that this population expands as tumors continue to progress and evolve over time (Fig. 5B). Age, histology subtypes, and CD8 TIL density were studied across the 35 NSCLC cases and were homogeneously distributed (Supplementary Fig. S10A). Additionally, we did not observe any association between these variables and Ebo abundance (Supplementary Fig. S10B and S10C). We did observe that, in advanced NSCLC

Figure 3. Ebo $CD8^+$ TIL is a transcriptionally distinct and dysfunctional subset. **A,** Heat map showing differentially expressed genes between Em and Ebo $CD8^+$ TIL subsets. **B,** Volcano plot of upregulated genes in Em over Ebo (left) or Ebo over Em (right) $CD8^+$ TIL population. Each red or green dot denotes an individual gene with adjusted $P < 0.01$ (two-sided moderated *t*-test) and fold change ≥ 2. DEG, differentially expressed gene. **C,** GSEA plot showing an enrichment of cycling signatures in the Ebo population and stem-cell signatures in the Em population. The color scale indicates the expression score in the indicated subset, and the square size indicates the 1-FDR. Proliferation: 1, GNF2 MKI67; 2, GNF2 SMC2L1; 3, GNF2 ESPL1; 4, GNF2 CENPE; 5, GNF2 CCNA2; 6, Eguchi cell-cycle RB1 targets; 7, Whitfield cell-cycle literature; 8, GO DNA replication-dependent nucleosome organization; 9, Rosty cervical cancer proliferation cluster. Stemness: 10, Piccaluga angioimmunoblastic lymphoma up; 11, Jaatinen hematopoietic stem cell DN; 12, Wong adult tissue stem module; 13, Harris brain cancer progenitors; 14, Hallmark angiogenesis. **D,** Representative GSEA of cycling genes signature: GNF2 MKI67 (left panel) and hematopoietic stem cell genes signature: Jaatinen hematopoietic stem cell DN (right panel) with the highest enrichment score (EC). **E,** TCRβ clonalities are shown by whisker plots, where the lines indicate median values and the boxes indicate interquartile range (IQR) values. Data from sorting cell subset sequence results that are over 10% frequency clonalities of Ebo, Em, and Eff are shown. **F,** The relative abundance of TCRβ clonotypes of Ebo, Em, and Eff. The large clonalities range from 10% to 100%, the medium clonalities range from 1% to 0.1%, and the small clonalities range is lower than 0.1%. The clonotypes are shown from all sorting cell subsets combined together. **G,** Bar plot depicts the percentage of $IFN\gamma^+$ cells from sorted Ebo, Em, and Eff $CD8^+$ TIL subsets cultured for 12 hours with (red) or without (black) PMA plus ionomycin, obtained from patients with NSCLC ($n = 9$). **H,** Bar plot depicts the cleaved caspase-3 expression levels in Ebo, Em, and Eff $CD8^+$ TILs from 35 NSCLC tumors analyzed by multiplex-QIF. **I,** GSEA plot showing an enrichment of apoptosis signatures in the Ebo population over the Em (left) and Eff (right) subsets. *, $P < 0.05$; **, $P < 0.01$; ***, $P < 0.001$; ****, $P < 0.0001$.

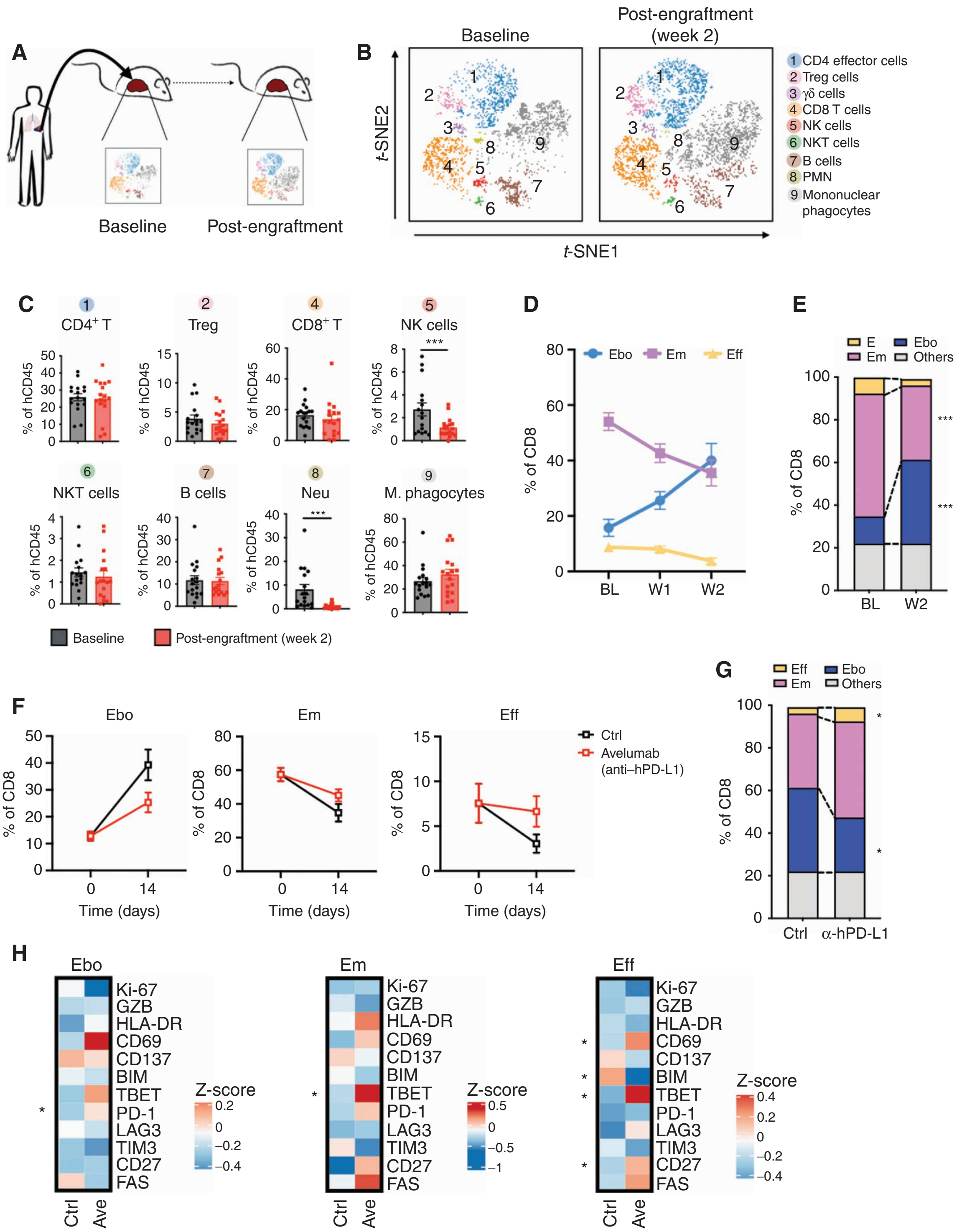

Figure 4. The B7-H1/PD-1 pathway mediates Ebo CD8+ TIL expansion within the human TME. **A,** Scheme of immune-PDX experiments. Patient-derived lung tumor xenografts were engrafted in NOD/SCID IL2R$\gamma^{-/-}$ (NSG) mice. Tumor tissue was digested and analyzed by mass cytometry at baseline and 2 weeks after engraftment. **B,** viSNE analysis depicts tumor xenograft-infiltrating leukocytes at baseline and 2 weeks after engraftment in NSG mice. Each immune subset is identified with a different color and a number. **C,** Frequency of depicted tumor xenograft-infiltrating leukocyte populations at baseline (gray) and 2 weeks after (red) engraftment. **D,** Percentage of Ebo, Em, and Eff of total tumor-infiltrating CD8+ T cells at baseline and at week 1 and week 2 after engraftment. **E,** CD8 composition with the different CD8+ TIL subsets at baseline and at week 2 after engraftment. **F,** Percentage of Ebo, Em, and Eff of total tumor-infiltrating CD8+ T cells from control and avelumab-treated mice at baseline and at week 2 post-engraftment. **G,** CD8+ T-cell composition within the different CD8+ TIL subsets from control and avelumab-treated mice at week 2 post-engraftment. **H,** Heat map showing differentially expressed proteins in Em, Ebo, and Eff CD8+ TIL subsets from control and avelumab-treated mice. hPD-L1, human PD-L1; Neu, neutrophils; M. phagocytes, mononuclear phagocytes.

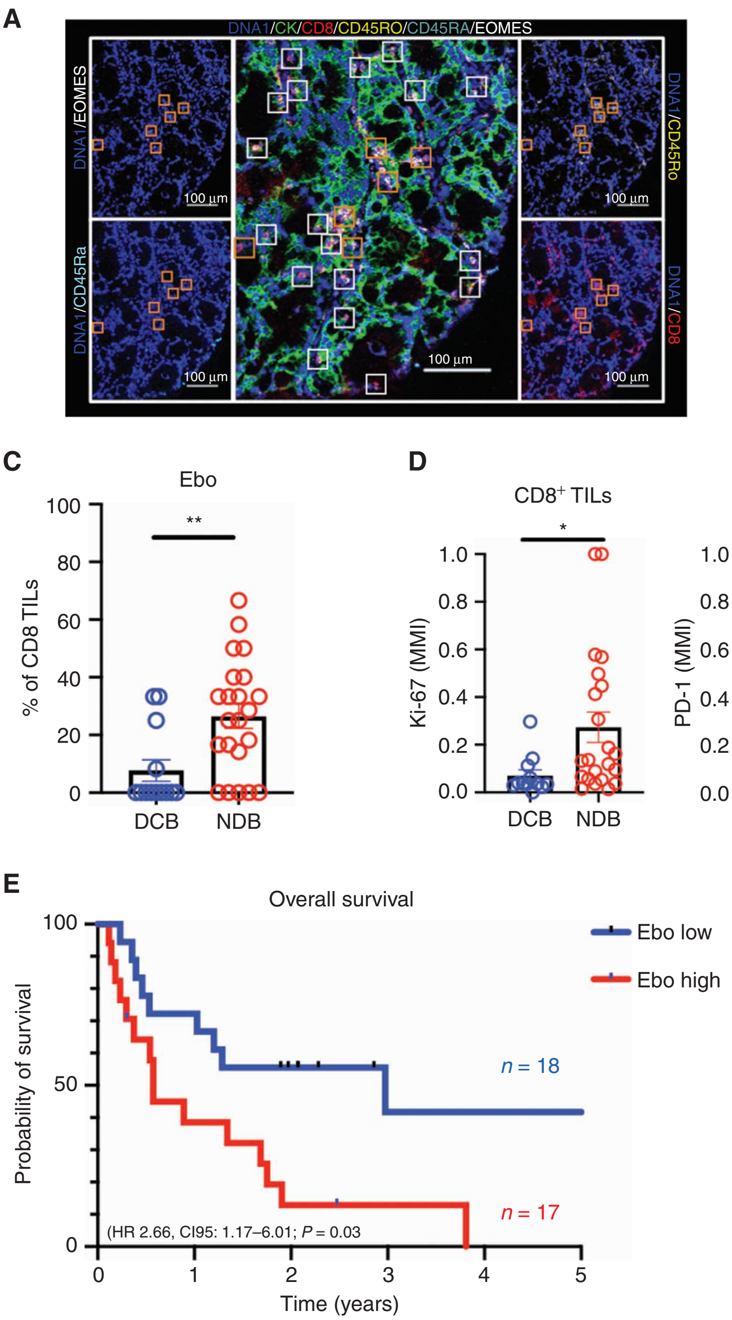

Figure 5. Ebo $CD8^+$ TIL abundance is associated with tumor development and resistance to anti-PD therapy in patients with NSCLC. **A,** Representative image showing IMC staining of a NSCLC case and Ebo $CD8^+$ TIL identification strategy. Each marker is represented by a different color as indicated in the panel. Orange squares indicate the Ebo $CD8^+$ TILs selected based on $CD8^+CD45RO^+CD45RA^-EOMES^+$ expression of the markers. White squares indicate non-Ebo $CD8^+$ TILs. **B,** Percentage of Ebo $CD8^+$ population over total $CD8^+$ TILs in clinical stages I (*n* = 12), II (*n* = 12), III (*n* = 16), and IV (*n* = 18). **C,** Bar-dot plots depict percentages of Ebo $CD8^+$ TIL population over total $CD8^+$ TILs in patients with durable clinical benefit (DCB; *n* = 13) or non-durable clinical benefit (NDB; *n* = 22) from anti-PD therapy. **D,** Quantification of Ki-67, PD-1, and LAG3 CD8 TIL expression in patients with DCB and NDB from anti-PD therapy. **E,** Kaplan–Meier survival curves for 35 patients with NSCLC treated with anti-PD therapy. Patients were divided in two groups based in tumors harboring Ebo ≥ 17.5% (high) or Ebo < 17.5% (low) of total CD8 TILs. *P* values were determined by the log-rank test. *, $P < 0.05$; **, $P < 0.01$; ***, $P < 0.001$; ****, $P < 0.0001$.

cases, the presence of tertiary lymphoid structures was associated with an ~2.5-fold lower Ebo $CD8^+$ TIL proportion, but this difference did not reach statistical significance (Supplementary Fig. S10D and S10E). Finally, consistent with previous observations by QIF, we identified among advanced NSCLC cases a CD8 TIL cluster coexpressing cleaved caspase-3, CD45RO, EOMES, Ki-67, PD-1, LAG3, and TIM3 (Supplementary Fig. S11). Importantly, patients with non-durable clinical benefit (NDB) to anti-PD therapy showed a significantly higher proportion of the Ebo $CD8^+$ TIL subset than patients with durable clinical benefit (DCB) in baseline tumor samples ($P = 0.004$; Fig. 5C). Alternative Ebo CD8$^+$ TIL gating strategies including Ki-67 protein expression were used to confirm this result (Supplementary Fig. S12A–S12C). Consistent with this finding, patients with NDB also showed CD8$^+$ TILs with higher PD-1, LAG3, and Ki-67 expression, markers associated with the Ebo CD8$^+$ TIL phenotype (Fig. 5D). Finally, Ebo CD8$^+$ TIL subset abundance was associated with a worse overall survival (hazard ratio = 6.08; 95% confidence interval, 2.57–5.25; $P < 0.05$) in patients with NSCLC treated with anti-PD therapy (Fig. 5E). A multivariate analysis including PD-L1 expression as a covariate identified Ebo CD8$^+$ TIL abundance as an independent predictor of outcome (Supplementary Table S3). Taken together, our findings support the suggestion that Ebo is expanded in the TME of patients with advanced NSCLC, and its expansion is independently associated with reduced efficacy of anti-PD therapy.

DISCUSSION

The basis of T-cell dysfunction in cancer and the best way to overcome it remain incompletely understood. One of the main hurdles to achieving greater understanding has been the use of low-resolution phenotypical technologies and the lack of suitable *in vivo* experimental models to investigate the human immune TME. Here, we used multiparametric single-cell mass cytometry and tissue imaging technology tools combined with a lung cancer humanized immune-PDX model to explore CD8$^+$ TIL diversity and its response to immunotherapy. We identified three phenotypically, transcriptionally, and functionally distinct CD8$^+$ TIL subsets: Eff, Em, and Ebo. The Ebo subset is characterized by a burned-out dysfunctional phenotype and specifically expands within the TME in a PD-pathway–dependent manner. Furthermore, Ebo progressively accumulates in patients with advanced NSCLC and is associated with primary resistance to anti-PD therapies. Our findings suggest that this CD8$^+$ TIL population may contribute to a less responsive immune TME and provide insights into the development of future T cell–based cancer immunotherapies.

To phenotypically characterize CD8$^+$ TILs, we employed single-cell mass cytometry technology, which allowed us to multiplex 39 markers per cell. Different methods of analysis have been designed over the past few years to maximize this multidimensional single-cell data (28). Here, we used CITRUS, a method specifically designed to identify and compare hierarchical clusters between groups of samples in an unsupervised manner. Using this method, we compared paired Tu and non-Tu lung tissue for immune cell composition. This approach resulted in fundamental findings: (i) lymphoid cells, but not myeloid cells, are preferentially expanded in lung tumor tissues; (ii) CD8$^+$ TILs are highly proliferative in contrast to non-Tu tissue-infiltrating CD8$^+$ T cells; and (iii) three major CD8$^+$ TIL subsets were identified, but only one of them, Ebo, was expanded in the TME (Fig. 2E). In contrast, the other two CD8$^+$ TIL subsets were either diminished (Eff) or unchanged (Em) in the TME compared with adjacent non-Tu lung tissue. More importantly, we found that, whereas Ebo represents 10% to 15% of the total CD8$^+$ TILs in early-stage NSCLC, its abundance rises to 30% to 40% in advanced NSCLC, indicating a higher relevance of this compartment in late-stage disease (Fig. 5B).

To demonstrate the dynamic evolution of Ebo within the TME and its response to immunotherapy, we developed a previously undescribed immune-proficient PDX model, referred to as the immune-PDX model. In contrast to conventional immune-deficient PDX models, immune-PDX retains an intact patient-derived tumor immune microenvironment (Fig. 4A and B). Fresh patient-derived lung tumor xenografts are engrafted into severely immunodeficient mice and contain all the original components of the growing tumor in the patient, including hematopoietic, stromal, and tumor cells. Although fibroblasts, neutrophils, and natural killer cells are progressively replaced by murine stroma cells, all human lymphoid populations remain stable during the first 2 weeks after engraftment, supporting their modulation and study. When TILs are studied in patient samples, a challenging aspect is that new T cells are continuously arriving at the TME site, making it difficult to know which CD8$^+$ subsets have just arrived and which have been differentiated within the TME. Because we recreated the patient TME in a T cell–deficient host, one of the main advantages of this model is that the evolution and reactions of TIL subsets can be analyzed without the interference of “newcomers.” In this context, we demonstrated that the Ebo CD8$^+$ TILs were progressively expanded within TME over time. More interestingly, we found that Ebo expansion was minimized when mice were treated with avelumab (clinical grade anti–B7-H1 mAb), indicating that the PD pathway is required for the expansion of this population. Although the contribution of the PD pathway to a CD8 subset expansion seems to be contradictory with prior reports suggesting that PD-1 transmits a signal to suppress T-cell proliferation (29, 30), it is important to consider that these studies employed polyclonal and heterogeneous T cells. It is still possible that the PD pathway provides a proliferative signal for a subset of T cells, which is consistent with our earlier work showing that B7-H1 could be costimulatory for human T cells (31). Supporting this hypothesis, it has been recently reported that PD-1 silencing inhibits the proliferative activity of chimeric antigen receptor modified T cells (32). It remains to be clarified, however, whether the observed expansion of Ebo associated with the PD pathway is due to a selective proliferative stimulus or if, instead, the B7-H1/PD-1 blockade is preventing the conversion of other populations into Ebo. The fact that clonality was low and clonotype diversity high in the Ebo compartment further supports the idea that the expansion of this compartment is more dependent on the conversion of other populations into Ebo.

Dysfunctional CD8$^+$ T-cell subsets have been previously described in the TME (33). The most frequently used term to designate these cells has been “exhausted” T cells, imported from chronic viral infections lymphocytic choriomeningitis virus. The Ebo CD8$^+$ TILs in our study are also dysfunctional and share several features with exhausted T cells, including coexpression of coinhibitory receptors (PD-1, LAG3, and TIM3), loss of IFNγ production upon restimulation, and a terminally differentiated phenotype (EOMES^{hi}TBET^{lo}). However, in contrast with the classic exhausted phenotype, Ebo is highly proliferative. This intriguing result is supported by two recent studies showing a highly proliferative dysfunctional CD8$^+$ TIL subset in the TME of patients with melanoma and NSCLC (9, 10). In our case, this dysfunctional population is characterized not only by a highly proliferative signature but also by the highest expression of activation markers such as CD45RO, CD27, PD-1, LAG3, TIM3, CD28, and FAS, suggesting that these cells may be pushed beyond the threshold of optimal activation. Supporting this interpretation, we previously demonstrated that patients with NSCLC with KI-67^{hi} and/or $GzmB^{hi}$ $CD8^+$ TILs are associated with worse response to cancer immunotherapy (34). Other groups have suggested that an overactivation of $CD8^+$ TILs may be counterproductive, due to an excess of IFNγ (35) or TNFα (36) that may lead to T-cell death programs, thereby compromising the antitumor response. In this regard, we have observed that the Ebo population is characterized by the highest FAS and cleaved caspase-3 levels compared with the other $CD8^+$ TIL subsets, reinforcing the interpretation of apoptotic hyperactivated $CD8^+$ TILs. Given these distinctions from previously described exhausted TILs, we have proposed the term “burned-out” T cells to more accurately reflect the overactive and apoptotic phenotype of these cells. Importantly, blockade of the PD pathway reduced BIM and cleaved caspase-3 in activated Eff $CD8^+$ TILs (Fig. 4H). Collectively, our results suggest that anti-PD therapy may be preventing activated T cells from entering into an apoptotic death program rather than restoring the function of exhausted/dysfunctional T cells. Although these findings require further confirmation, they are consistent with previous studies reporting that anti-PD therapies may be promoting the expansion and preventing the deterioration of a stem-like $CD8^+$ TIL subset, identified as PD-1^+Tcf1^+, rather than restoring exhaustion (37–40).

T cell–inflamed tumors with abundant Ebo $CD8^+$ TILs may be refractory to cancer immunotherapy due to an excess of irrecoverable apoptotic TILs, as previously suggested (41, 42), potentially competing for space and resources with other $CD8^+$ TIL populations. Along these lines, a recently published study showed an association between higher T-cell infiltration and higher terminally exhausted $CD8^+$ T cells, indicating that the greater the T cell accumulation in tumors, the greater the likelihood of becoming dysfunctional (40). One interpretation of these results is that a lack of T-cell homeostasis and an excess of activated ineffective TILs may be responsible for impaired T-cell responses in some patients. If this is the case, T-cell enhancer strategies (e.g., bispecific T-cell engagers) may be detrimental, and strategies designed to protect activated T cells from apoptosis may be needed instead. An alternative interpretation of these results may be that the Ebo compartment must be depleted to provide space and resources to the cells with greater efficacy such as Eff $CD8^+$ TIL subsets. In this regard, a potential benefit of concomitant chemotherapy or radiotherapy may be the clearance of the Ebo compartment.

Taken together, our data illustrate a previously unrecognized category of anti-PD–resistant T-cell inflamed tumors. Contrary to expectations, the underlying mechanism of resistance may be an excess of dysfunctional activated TILs. This work may contribute to a deeper understanding of T cell–inflamed tumor diversity, and Ebo may serve as a useful tissue biomarker with implications for the development of future T cell–based cancer immunotherapies.

METHODS

Patients and Samples

Fresh tumor samples were prospectively collected from individuals with NSCLC undergoing primary surgical treatment between August 2015 and February 2018 at the Yale Cancer Center, New Haven, CT. After surgery, tumor and tumor-free sections (identified and supervised by a pathologist) were collected from each patient and processed in the first 2 hours after being surgically removed. Tumor-free fragments were collected at least 5 cm away from the macroscopic tumor border. Tumor and tumor-free fragments were reviewed by a licensed pathologist (K.A. Schalper) to confirm the diagnosis and quality of the samples. One tumor sample was identified as sarcoidosis, and one tumor-free sample was found to include areas of active pneumonia. Both of these cases were processed but not included in the analysis. For each specimen, a fragment was fixed in 10% neutral-buffered formalin and paraffin-embedded for histopathologic analysis. The remainder of the tissue was directly processed for single-cell CyTOF analysis (Supplementary Fig. S1). When tumor tissues were bigger than 10 mm^3, an additional fragment of the tumor tissue was engrafted in immunodeficient NSG mice to establish a short-term PDX. The clinical and pathologic characteristics of these patients are described in Supplementary Table S4. Additionally, we included retrospectively collected formalin-fixed, paraffin-embedded tumor samples from patients with stage IV NSCLCs treated with single-therapy anti-PD agents at the Yale Cancer Center between 2011 and 2017. These cases were represented in a tissue microarray (TMA) format, each containing two independent 0.6-mm tumor cores. The TMAs were constructed by selecting areas containing viable tumor cells and stromal elements on hematoxylin and eosin–stained preparations (as assessed by a licensed pathologist) and without enriching for specific tumor regions, tissue structures, or immune-related features. The clinical and pathologic characteristics of these patients are described in Supplementary Table S4 and treatment characteristics in Supplementary Table S5. All tissues were used with each patient’s written informed consent or, in some cases, a waiver of consent, after approval from the Yale Human Investigation Committee (protocols 1412015109, 9505008219, and 1608018220) and conducted in accordance with the tenets of the Declaration of Helsinki.

Antibodies

All metal-conjugated antibodies were either purchased preconjugated from Fluidigm or purchased purified and conjugated in-house using mass cytometry antibody conjugation kits from Fluidigm according to the manufacturer’s instructions. For details, see Supplementary Tables S1 and S2. The following antibodies were developed, produced, and quality controlled at Pfizer facilities: avelumab (a fully human IgG1 anti-human PD-L1) and irrelevant human IgG1 as an isotype-matched control.

Mice

Female NOD/SCID IL2R$\gamma^{-/-}$ (NSG) mice 6 to 8 weeks old were purchased from The Jackson Laboratory. All mouse protocols were in accordance with NIH guidelines and approved by the Animal Care and Use Committee of Yale University School of Medicine (reference 2013-11387 approval).

CyTOF Sample Preparation

A total of 1×10^6 to 3×10^6 suspension cells from each Tu or non-Tu lung tissue were incubated with antibodies against CD16/32 at 50 mg/mL for 10 minutes at room temperature to block Fc receptors. Subsequently, metal-conjugated mAb cocktails against cell surface molecules were added, and further incubated for 20 minutes on ice (see details in Supplementary Table S1). Cells were stained for viability with 5 mmol/L cisplatin in FBS (Fluidigm) for 1 minutes at 4°C. After the treatment with the Fixation/Permeabilization Buffer (Thermo Fisher), cells were further incubated with the metal-conjugated mAb cocktails against intracellular proteins (see details in Supplementary Table S1). Then, cells were washed and stained with 1 mL of 1:4000 $^{191/193}$Ir DNA intercalator (Fluidigm) diluted in phosphate-buffered saline (PBS) containing 1.6% paraformaldehyde (Electron Microscopy Sciences) and stored at 4°C until acquisition.

Single-Cell Mass Cytometry Sample Acquisition

Samples were acquired in a Helios machine (Fluidigm). At the moment of acquisition, cells were washed once with PBS with 0.5% bovine serum albumin (BSA) and 0.02% NaN_3 and once with double-distilled water (ddH_2O); they were then resuspended in ddH_2O containing bead standards (Fluidigm) to approximately 10^6 cells/mL. Subsequently, samples were acquired at an event rate of <400 events per second.

Antibody Validation and Titration for Single-Cell Mass Cytometry

Isolated human PBMCs were stimulated with a concentration of 0.5 μg/mL plate-bound anti-CD3 (OKT3) and 2 μg/mL soluble anti-CD28 (28.2; eBioscience) for 72 hours or cultured in medium—RPMI 1640 with 10% FBS (PAN-Biotech), 1 mmol/L sodium pyruvate (Sigma), and 100 ng/mL penicillin/streptomycin—for the same period of time. Unstimulated PBMCs were used as a negative control for antibody titration and staining protocol optimization. The optimal antibody concentration was assayed by serial dilutions and determined by the obtained median mass intensity signal-to-noise ratio from internal positive and negative controls (see details in Supplementary Fig. S2). Additionally, in each CyTOF experiment unstimulated and stimulated PBMC samples were included as internal reference.

Multiplexed QIF

Using previously validated and standardized multiplexed QIF panels and serial TMA sections (43), we measured the levels of cytokeratin (clone AE1/AE3; eBioscience), PD-L1 (B7-H1, clone 405.9A11; Cell Signaling Technology), CD4 (clone SP35; Spring Bioscience), CD8 (clone C8/144B; Dako), CD20 (clone L26; Dako), CD68 (clone KP1; Dako), CD45RO (clone UCHL1; BioLegend), and CD45RA (clone HI100; BioLegend). Cleaved caspase-3 (clone D3E9; Cell Signaling Technology) was validated and standardized using Jurkat cells treated with dimethyl sulfoxide (untreated) or 1 μmol/L of camptothecin (treated) for 18 hours to induce apoptosis (see details in Supplementary Fig. S8A and S8B). Freshly cut TMA serial sections were deparaffinized, and antigen retrieval was performed using an EDTA buffer (Sigma-Aldrich), pH 8; they were then heated for 20 minutes at 97°C in a Lab Vision PT Module (Thermo Fisher Scientific). Endogenous peroxidase activity was inactivated by incubating the TMA section in a solution containing 0.3% hydrogen peroxide in methanol for 20 minutes, followed by incubation in a blocking solution containing 0.3% BSA in 0.05% Tween solution for 30 minutes. An antibody cocktail was used for the primary target detection, followed by a secondary detection using the specific horseradish peroxidase–conjugated IgG anti-isotype. Tyramide signal amplification with tyramide-based fluorescent reagents (PerkinElmer) was utilized for signal amplification and detection. Sections were washed twice with a 100 mmol/L benzoic hydrazide solution in between antibody incubation periods to eliminate residual horseradish peroxidase activity. Nuclei staining was performed with 4′,6-diamidino-2-phenylindole (DAPI). Fluorescence signal was measured quantitatively using the AQUA method for QIF. Samples with tissue or staining artifacts by visual examination were excluded.

IMC Sample Preparation

For IMC staining, antibodies were optimized using QIF as a gold standard and a control array including negative and positive controls, as well as cases with a range of expression for each marker. Fluorescence signal quantification was performed using the AQUA method of QIF. Each slide was visually examined to exclude samples with tissue/staining artifacts and those with less than 5% tumor content. Cases were considered to display detectable levels of each target when the QIF score was above the signal-to-noise threshold determined by measuring negative control preparations and by visual examination of the sample. For IMC staining, a comparable and compatible staining protocol was designed based on the QIF gold standard. Briefly, fresh TMA serial sections were deparaffinized, and antigen retrieval was performed using an EDTA buffer (pH 9) and heating for 20 minutes at 97°C in a Lab Vision PT Module. The EDTA solution was rinsed twice using Tris-buffered saline (TBS) solution, followed by incubation in a blocking solution containing 0.3% BSA in 0.05% Tween solution for 30 minutes. Tissue was covered with a cocktail of 26 metal-conjugated antibodies prepared in blocking solution. After 1 hour of primary incubation at room temperature, tissues were rinsed twice using a solution containing 0.025% Tween 20 in TBS solution to remove nonspecific antibody staining. DNA and membranes were costained using a solution containing 1 μmol/L pooled ^{191}Ir and ^{193}Ir, and 1 μg/mL ^{115}In LipoR in TBS for 1 hour at room temperature. The costaining solution was rinsed using Tween 20 and the TBS solution followed by two washes for 1 minute each using ddH_2O. The slide was finally air-dried for 60 minutes and stored until analysis.

IMC Sample Acquisition

For IMC analysis and instrument settings, the Hyperion machine from the Yale IMC core facility was used for all the studies described here. The mass cytometer and scanner were tuned every day at 20 Hz and 0 dB of laser intensity using a commercial tuning slide provided by Fluidigm. The tuning reference values used as a quality control for a working day were 2.37% ± 0.34% and 0.42% ± 0.11% for transient cross-talk 1 and 2, respectively, and for Lu(175) mean duals above 900. All tissue samples and cells were ablated at 5 dB and 200 Hz; an area of 750 × 750 μm was always considered for TMA spots and a smaller area of 100 × 100 μm for titrations. TMA slides were scanned using the batch tool. A panoramic view of the whole slide was uploaded, and a macro region of interest was created covering the tissue spot grid. On the created working area, each spot was selected based on the map layout of each TMA. A protocol was assigned and carried out until 20 spots were completed for a 24-hour continuous scan. No more than 25 cases were programmed to be scanned per tuning event.

Antibody Validation and Titration for IMC

For IMC validation and optimization, specificity, and sensitivity, the optimal titer was calculated separately for metal-conjugated and unconjugated versions of each antibody. The optimal antibody concentration was assayed by serial dilutions and determined by the obtained QIF scores and the signal-to-noise ratio from internal positive and negative control tissues (percentile p90 to percentile p10). Cytokeratin and vimentin were assayed in combination to confirm selective exclusion staining patterns for further tissue segmentation. Antigen retrieval conditions were optimized, and QIF was performed using 1 mmol/L EDTA (pH 8) and 10 mmol/L citrate (pH 6) independently. The detection limit was optimized by comparing the dynamic range for each condition.

Immune-PDX Tumor Model

Surgical specimens from primary lung carcinomas were implanted subcutaneously into the flank of 8 to 10 female NSG mice at 6 to 8 weeks of age per experiment. Mice were treated intraperitoneally with anti-hPD-L1 mAbs (avelumab) or isotype control at days 5 and 10 post-implantation. At day 7 or 14, mice were sacrificed, and tumors were collected for analysis.

Human TIL and PBMC Isolation

Human TILs were derived from original patient tumors, as well as tumor tissue from each immune-PDX model after treatment. TILs were obtained by processing tumor tissue with a gentleMACS Dissociator (Miltenyi Biotec) in the presence of RPMI 1640 with 0.5% BSA and 5 mmol/L EDTA. Cell suspensions were filtered using a 70-µm cell strainer (BD Falcon), centrifuged at 600*g* for 7 minutes at 4°C, and resuspended in PBS with 0.5% BSA and 0.02% NaN_3, and were then ready for analysis. Human PBMCs were purified from buffy coats of healthy donors using Ficoll-Hypaque (Sigma-Aldrich) gradient centrifugation, according to the manufacturer's instructions.

TIL Sorting

For isolation of Ebo, Em, and Eff $CD8^+$ TIL subsets, 1×10^6 to 2×10^6 tumor-infiltrating leukocytes were resuspended in 200 µL staining buffer containing fluorophore-conjugated mAb cocktail against human cell-surface molecules: CD45 BV510 (clone HI30), CD8 PerCP-Cy5.5 (clone RPA-T8), CCR7 BV421 (clone G043H7), CD45RO PE (clone UCHL1), and CD45RA PE-Cy7 (clone HI100). After a 20-minute incubation at 4°C, cells were washed twice, and cell sorting was performed using a BD FACS Aria III (BD Biosciences). We trained a gating strategy to sort the subsets most similar to those identified by CITRUS. We first trained this strategy using our current CyTOF data doing manual gating and comparing the expression profile of the three subsets identified by CITRUS and the three subsets defined by manual gating (Supplementary Fig. S13A and S13B). After we confirmed that our manual gating strategy was able to identify subsets similar to those identified by CITRUS, we designed a similar strategy for the FACS (Supplementary Fig. S13C). Furthermore, after we sorted the cells, we tested whether or not the expression profile of the sorted subsets was comparable to that of the clusters defined by CITRUS (Supplementary Fig. S13D). Approximately 1×10^4, 1.5×10^4 to 2×10^4, and 0.5×10^4 to 1×10^4 of Ebo, Em, and Eff cells, respectively, were sorted as an average across experiments. In three experiments cells were directly sorted in lysis buffer RLT (RNeasy Micro Kit, 74004; QIAGEN) which already contained beta-mercaptoethanol and dithiothreitol, and total RNA was extracted from the lysed cells using the RNeasy Micro Kit protocol. Total RNA samples were submitted to the Yale Center for Genome Analysis (YCGA) where they were analyzed for quality control and RNA-seq. In the remainder of experiments, cells were cultured *in vitro* for T-cell stimulation experiments.

T-cell Stimulation In Vitro

From nine lung tumor samples, Ebo, Em, and Eff $CD8^+$ TIL subsets were stimulated with 50 ng/mL PMA and 1 µg/mL ionomycin (BD Biosciences) for 6 hours. Two hours before the end of the PMA–ionomycin stimulation, 1× monensin and 1× brefeldin A (eBioscience) were added for intracellular IFNγ staining. For analysis of IFNγ intracellular levels, cells were fixed and permeabilized using the Fix/Perm solution (eBioscience) for 30 minutes at room temperature. After they were washed twice, cells were resuspended in 1× Permeabilization Buffer (eBioscience) containing fluorescein isothiocyanate–conjugated anti-IFNγ antibodies (clone 25723.11) for 15 minutes at room temperature. The acquisition of samples was carried out on an Attune NxT Flow Cytometer (Thermo Fisher Scientific).

CyTOF Data Analysis

All mass cytometry files were normalized together using the mass cytometry data normalization algorithm (44). For analysis, FCS files were manually pregated on $^{193}Ir\ DNA^+CD45^+$ events, excluding cisplatin-positive dead cells, doublets, and DNA-negative debris, by Cytobank. The gated $CD45^+$ population was then clustered based on all labeled phenotypic markers using visualization (viSNE; ref. 45) or hierarchical clustering (CITRUS; ref. 27) methods. CITRUS is comprised of several steps: (i) Cells from samples are combined and clustered in a semi-unsupervised manner to automatically identify clusters of related cells. (ii) Descriptive statistics characterizing various properties of each cluster (cluster features) are extracted on a per-sample basis. (iii) Extracted cluster features are used in conjunction with a user-specified endpoint of interest to train a supervised model. (iv) Internal cross-validation is used to evaluate model fit and select the appropriate regularization threshold for a final model. Finally, (vi) model features are plotted as a function of endpoint of interest, and cluster phenotypes are determined by density plots of markers used for clustering. An equal number of events (or a subset of events) from all samples are randomly selected and then combined and clustered using agglomerative hierarchical clustering, producing groups of phenotypically similar cells. The dissimilarity between any two cells was specified by the Euclidean distance between clustering markers, and Ward's linkage was used as the agglomeration method. Rather than cutting the dendrogram at a fixed height to identify clusters, all clusters in the hierarchy of merged clusters larger than a user-specified size were retained for subsequent analysis.

IMC Data Analysis

A supervised phenotyping and segmentation analysis was developed using the IMC viewer provided by Fluidigm. For imaging studies and staining pattern comparisons, each metal channel was visualized and the image quality was optimized using gain and thresholds range tools. Integrated dual histograms were used as a reference for signal normalization to avoid saturated pixels and for comparing with a pathologist's validated immunofluorescence pattern. After fixing all parameters for the visualization of each stained marker, a supervised identification of T lymphocytes, macrophages, and tumor cells was performed based on morphology and the specific cluster of differentiation for lymphocytes CD4 (156Gd), CD8 (162-Dy), CD20 (161-Dy), CD68 (159Tb), and pan-cytokeratin (148Nd) for tumor cells. All scanned regions of interest included a total of 20 cells per field of view from a TMA batch and were analyzed in the same manner. The selected positive pixels for a marker were indicated as single cells. The integrated counts were exported as a TXT file, and the composed images were saved for further studies. The integral counts for each marker were normalized by the mean level of ^{132}Xe and ^{133}Xe detected in each cell compartment. This allowed us to account for the different areas covered by cells of different shapes and sizes, as the Xe ion is uniformly detected in tissue due to impurities in the argon plasma source. The Ebo, Em, and Eff CD8 TIL compartments identified by IMC were based in the combination of CD8, CD45RO, CD45RA, and EOMES markers, using the following approach: Ebo ($CD8^+$, $CD45RO^+$, $CD45RA^-$, and $EOMES^+$), Em ($CD8^+$, $CD45RO^+$, $CD45RA^-$, and $EOMES^-$), and Eff ($CD8^+$, $CD45RO^-$, and $CD45RA^+$). The expression profile of each compartment was determined to evaluate consistency with the clusters identified by CITRUS (Supplementary Fig. S14).

RNA-seq Data Analysis

RNA samples were submitted to the YCGA, and the libraries were constructed by YCGA protocols (https://medicine.yale.edu/keck/ycga/Images/9_tcm240-21599.pdf). The libraries underwent 101-bp paired-end sequencing using an Illumina HiSeq 2500 according to Illumina protocols. Low-quality reads were trimmed and adaptor contamination was removed using Trim Galore (v0.5.0). Trimmed reads were mapped to the human reference genome (hg38) using HISAT2 (v2.1.0) (46). Gene expression levels were quantified using StringTie (v1.3.3b) (47) with gene models (v27) from the GENCODE project. Differentially expressed genes were identified using DESeq2 (v1.22.1) (48).

TCR Sequencing Data Analysis

T-cell receptor β-chain clonality was assessed using the MiXCR tool using standard parameters of the RNA-seq workflow. TCR clonality was analyzed using the R package immunarch (http://doi.org/10.5281/zenodo.3367200).

Statistical Analysis

Student *t* test, two-way analysis of variance, and log-rank tests on GraphPad Prism 8.0 for macOS were used for statistical analysis. CD8 and Ebo abundance cutoff points were determined using the median values across all samples. Multivariate analysis was performed using the Cox proportional hazards regression model on SPSS Statistics for Windows. Statistical significance was considered to be $P < 0.05$. P values were reported as follows: NS, not significant; *, $P < 0.05$; **, $P < 0.01$; ***, $P < 0.001$; ****, $P < 0.0001$. The error bars in figures represent standard error of the mean (SEM).

Data Archive

The data have been archived at https://www.ncbi.nlm.nih.gov/geo and can be accessed under the study accession number GSE167235.

Authors' Disclosures

F. Villaroel-Espindola has received personal fees from Instituto Oncológico Fundación Arturo López Pérez outside the submitted work. T.K. Kim has received research funds from NextCure, American Cancer Society, American Society of Clinical Oncology, and the Edward P. Evans Foundation. I. Melero has received grants and personal fees from BMS, Roche, AstraZeneca, Bioncotech, and Alligator and personal fees from Pharmamar, Genmab, F-Star, Numab, Gossamer, and EMD outside the submitted work. R.S. Herbst receives consulting fees from the following: AbbVie Pharmaceuticals; ARMO Biosciences; AstraZeneca; Biodesix; Bolt Biotherapeutics; Bristol Myers Squibb; Candel Therapeutics, Inc.; Cybrexa Therapeutics; eFFECTOR Therapeutics, Inc.; Eli Lilly and Company; EMD Serono; Genentech/Roche; Genmab; Halozyme Therapeutics; Heat Biologics; I-Mab Biopharma; Immunocore; Infinity Pharmaceuticals; Loxo Oncology; Merck and Company; Mirati Therapeutics; Nektar; Neon Therapeutics; NextCure; Novartis; Ocean Biomedical, Inc.; Oncternal Therapeutics; Pfizer; Ribbon Therapeutics; Sanofi; Seattle Genetics; Shire PLC; Spectrum Pharmaceuticals; STCube Pharmaceuticals, Inc; Symphogen; Takeda; Tesaro; Tocagen; WindMIL Therapeutics; Xencor, Inc. R.S. Herbst received research support from AstraZeneca; Eli Lilly and Company; Genentech/Roche; Merck and Company. R.S. Herbst is a member of the board of directors (nonexecutive/independent) for Junshi Pharmaceuticals; Immunocore Holdings Limited. K.A. Schalper received grants from the National Cancer Institute–National Institutes of Health, Department of Defense, AACR/Stand Up To Cancer, AstraZeneca, and The Mark Foundation during the conduct of the study; has received personal fees from Clinica Alemana Santiago, Novartis, Moderna, Shattuck Labs, Pierre-Fabre, AstraZeneca, Ono Pharmaceuticals, AbbVie, Dynamo Therapeutics, EMD Serono, Torque Therapeutics, Agenus, Takeda, Genmab, Merck, Bristol Myers Squibb, PeerView, and Fludigm outside the submitted work; and has received grants from Navigate Biopharama, Tesaro/GSK, Moderna, Takeda Pharmaceuticals, Surface Oncology, Pierre-Fabre Research Institute, Merck, Bristol Myers Squibb, AstraZeneca, Ribon Therapeutics, and Eli Lilly outside the submitted work. L. Chen received grants from the National Cancer Institute–National Institutes of Health during the conduct of the study; has received grants from NextCure, DynamiCure, and Tayu outside the submitted work; and has received personal fees from Junshi, Zai Lab, Vcanbio, and GenomiCare outside the submitted work. No potential conflicts of interest were disclosed by the other authors.

Authors' Contributions

M.F. Sanmamed: Conceptualization, data curation, formal analysis, supervision, investigation, visualization, methodology, writing–original draft, writing–review and editing. **X. Nie:** Data curation, investigation, writing–review and editing. **S.S. Desai:** Resources, data curation, formal analysis, writing–review and editing. **F. Villaroel-Espindola:** Resources, data curation, formal analysis, investigation, methodology, writing–review and editing. **T. Badri:** Resources, data curation, formal analysis, investigation, methodology, writing–review and editing. **D. Zhao:** Resources, data curation, formal analysis, writing–review and editing. **A.W. Kim:** Resources, investigation, writing–review and editing. **L. Ji:** Resources, investigation, writing–review and editing. **T. Zhang:** Writing–review and editing. **E. Quinlan:** Investigation, writing–review and editing. **X. Cheng:** Investigation, writing–review and editing. **X. Han:** Writing–review and editing. **M.D. Vesely:** Resources, methodology, writing–review and editing. **A.F. Nassar:** Resources, data curation, formal analysis, methodology, writing–review and editing. **J. Sun:** Writing–review and editing. **Y. Zhang:** Writing–review and editing. **T.K. Kim:** Writing–review and editing. **J. Wang:** Data curation, writing–review and editing. **I. Melero:** Writing–review and editing. **R.S. Herbst:** Funding acquisition, project administration, writing–review and editing. **K.A. Schalper:** Resources, data curation, formal analysis, investigation, visualization, writing–review and editing. **L. Chen:** Conceptualization, resources, data curation, formal analysis, supervision, funding acquisition, writing–original draft, project administration, writing–review and editing.

Acknowledgments

We thank other members of L. Chen's Laboratory at Yale University for helpful discussions and technical assistance. We thank Maria Olguin for her support with figure design and Sarin Siriamnothep for her patience and support during preparation of this manuscript. This study was supported by the Mark Foundation for Cancer Research (19-029-MIA; R.S. Herbst and K.A. Schalper), Navigate Biopharma (K.A. Schalper), AstraZeneca (K.A. Schalper), Yale SPORE in Lung Cancer (P50CA196530; R.S. Herbst), Department of Defense–Lung Cancer Research Program (W81XWH-16-1-0160; K.A. Schalper), the National Institutes of Health (R03CA219603 and R37CA245154; K.A. Schalper), Stand Up To Cancer–American Cancer Society Lung Cancer Dream Team Translational Research Grant (SU2C-AACR-DT1715; R.S. Herbst and K.A. Schalper), and a Stand Up To Cancer–American Cancer Colorectal Cancer Dream Team Translational Research Grant (SU2C-AACR-DT22-17; K.A. Schalper). Stand Up To Cancer is a division of the Entertainment Industry Foundation. The indicated Stand Up To Cancer grants are administered by the American Association for Cancer Research, the scientific partner of Stand Up To Cancer. M.F. Sanmamed is supported by a Miguel Servet contract (MS17/00196) and a grant from Instituto de Salud Carlos III, Fondo de Investigacion Sanitaria (PI19/00668). M.D. Vesely is supported by a Physician-Scientist Career Development Award from the Dermatology Foundation, a Dermatology Fellow Award from the Melanoma Research Alliance, and a grant from the National Center for Advancing Translational Sciences (KL2 TR001862).

Received July 3, 2020; revised January 6, 2021; accepted February 26, 2021; published first March 3, 2021.

REFERENCES

1. Dong H, Strome SE, Salomao DR, Tamura H, Hirano F, Flies DB, et al. Tumor-associated B7-H1 promotes T-cell apoptosis: a potential mechanism of immune evasion. Nat Med 2002;8:793–800.
2. Taube JM, Anders RA, Young GD, Xu H, Sharma R, McMiller TL, et al. Colocalization of inflammatory response with B7-h1 expression in human melanocytic lesions supports an adaptive resistance mechanism of immune escape. Sci Transl Med 2012;4:127ra37.
3. Chen L, Han X. Anti-PD-1/PD-L1 therapy of human cancer: past, present, and future. J Clin Invest 2015;125:3384–91.
4. Sanmamed MF, Chen L. A paradigm shift in cancer immunotherapy: from enhancement to normalization. Cell 2018;175:313–26.
5. Sallusto F, Lenig D, Förster R, Lipp M, Lanzavecchia A. Two subsets of memory T lymphocytes with distinct homing potentials and effector functions. Nature 1999;401:708–12.

6. Barber DL, Wherry EJ, Masopust D, Zhu B, Allison JP, Sharpe AH, et al. Restoring function in exhausted CD8 T cells during chronic viral infection. Nature 2006;439:682–7.
7. Wherry EJ. T cell exhaustion. Nat Immunol 2011;12:492–9.
8. Wherry EJ, Kurachi M. Molecular and cellular insights into T cell exhaustion. Nat Rev Immunol 2015;15:486–99.
9. Thommen DS, Koelzer VH, Herzig P, Roller A, Trefny M, Dimeloe S, et al. A transcriptionally and functionally distinct PD-1+ CD8+ T cell pool with predictive potential in non-small-cell lung cancer treated with PD-1 blockade. Nat Med 2018;24:994–1004.
10. Li H, van der Leun AM, Yofe I, Lubling Y, Gelbard-Solodkin D, van Akkooi ACJ, et al. Dysfunctional CD8 T cells form a proliferative, dynamically regulated compartment within human melanoma. Cell 2019;176:775–89.
11. Azizi E, Carr AJ, Plitas G, Cornish AE, Konopacki C, Prabhakaran S, et al. Single-cell map of diverse immune phenotypes in the breast tumor microenvironment. Cell 2018;174:1293–308.
12. Zheng C, Zheng L, Yoo JK, Guo H, Zhang Y, Guo X, et al. Landscape of infiltrating T cells in liver cancer revealed by single-cell sequencing. Cell 2017;169:1342–56.
13. Kargl J, Busch SE, Yang GHY, Kim KH, Hanke ML, Metz HE, et al. Neutrophils dominate the immune cell composition in non-small cell lung cancer. Nat Commun 2017;8:1–11.
14. Simoni Y, Becht E, Fehlings M, Loh CY, Koo S-L, Teng KWW, et al. Bystander CD8+ T cells are abundant and phenotypically distinct in human tumour infiltrates. Nature 2018;557:575–9.
15. Chevrier S, Levine JH, Zanotelli VRT, Silina K, Schulz D, Bacac M, et al. An immune atlas of clear cell renal cell carcinoma. Cell 2017; 169:736–49.
16. Lavin Y, Kobayashi S, Leader A, Amir E ad D, Elefant N, Bigenwald C, et al. Innate immune landscape in early lung adenocarcinoma by paired single-cell analyses. Cell 2017;169:750–65.
17. Giesen C, Wang HAO, Schapiro D, Zivanovic N, Jacobs A, Hattendorf B, et al. Highly multiplexed imaging of tumor tissues with subcellular resolution by mass cytometry. Nat Methods 2014;11:417–22.
18. Jackson HW, Fischer JR, Zanotelli VRT, Ali HR, Mechera R, Soysal SD, et al. The single-cell pathology landscape of breast cancer. Nature 2020;578:615–20.
19. Jenkins RW, Aref AR, Lizotte PH, Ivanova E, Stinson S, Zhou CW, et al. Ex vivo profiling of PD-1 blockade using organotypic tumor spheroids. Cancer Discov 2018;8:196–215.
20. Neal JT, Li X, Zhu J, Giangarra V, Grzeskowiak CL, Ju J, et al. Organoid modeling of the tumor immune microenvironment. Cell 2018;175:1972–88.
21. Scognamiglio G, De Chiara A, Parafioriti A, Armiraglio E, Fazioli F, Gallo M, et al. Patient-derived organoids as a potential model to predict response to PD-1/PD-L1 checkpoint inhibitors. Br J Cancer 2019;121:979–82.
22. Sanmamed MF, Rodriguez I, Schalper KA, Onate C, Azpilikueta A, Rodriguez-Ruiz ME, et al. Nivolumab and urelumab enhance antitumor activity of human T lymphocytes engrafted in Rag2-/-IL2Rγnull immunodeficient mice. Cancer Res 2015;75:3466–78.
23. Rongvaux A, Willinger T, Martinek J, Strowig T, Gearty SV, Teichmann LL, et al. Development and function of human innate immune cells in a humanized mouse model. Nat Biotechnol 2014;32: 364–72.
24. Das R, Strowig T, Verma R, Koduru S, Hafemann A, Hopf S, et al. Microenvironment-dependent growth of preneoplastic and malignant plasma cells in humanized mice. Nat Med 2016;22:1351–7.
25. Jespersen H, Lindberg MF, Donia M, Söderberg EMV, Andersen R, Keller U, et al. Clinical responses to adoptive T-cell transfer can be modeled in an autologous immune-humanized mouse model. Nat Commun 2017;8:707.
26. Etxeberria I, Bolaños E, Quetglas JI, Gros A, Villanueva A, Palomero J, et al. Intratumor adoptive transfer of IL-12 mRNA transiently engineered antitumor CD8+ T cells. Cancer Cell 2019;36:613–29.
27. Bruggner RV, Bodenmiller B, Dill DL, Tibshirani RJ, Nolan GP. Automated identification of stratifying signatures in cellular subpopulations. Proc Natl Acad Sci U S A 2014;111:E2770–7.
28. Chattopadhyay PK, Winters AF, Iii WEL, Laino AS, Woods DM. High-parameter single-cell analysis. Annu Rev Anal Chem 2019;12:411–30.
29. Ribas A, Shin DS, Zaretsky J, Frederiksen J, Cornish A, Avramis E, et al. PD-1 blockade expands intratumoral memory T cells. Cancer Immunol Res 2016;4:194–203.
30. Tumeh PC, Harview CL, Yearley JH, Shintaku IP, Taylor EJM, Robert L, et al. PD-1 blockade induces responses by inhibiting adaptive immune resistance. Nature 2014;515:568–71.
31. Dong H, Zhu G, Tamada K, Chen L. B7-H1, a third member of the B7 family, co-stimulates T-cell proliferation and interleukin-10 secretion. Nat Med 1999;5:1365–9.
32. Wei J, Luo C, Wang Y, Guo Y, Dai H, Tong C, et al. PD-1 silencing impairs the anti-tumor function of chimeric antigen receptor modified T cells by inhibiting proliferation activity. J Immunother Cancer 2019;7:1–15.
33. Savas P, Virassamy B, Ye C, Salim A, Mintoff CP, Caramia F, et al. Single-cell profiling of breast cancer T cells reveals a tissue-resident memory subset associated with improved prognosis. Nat Med 2018; 24:986–93.
34. Gettinger SN, Choi J, Mani N, Sanmamed MF, Datar I, Sowell R, et al. A dormant TIL phenotype defines non-small cell lung carcinomas sensitive to immune checkpoint blockers. Nat Commun 2018;9:3196.
35. Pai CCS, Huang JT, Lu X, Simons DM, Park C, Chang A, et al. Clonal deletion of tumor-specific T cells by interferon-γ confers therapeutic resistance to combination immune checkpoint blockade. Immunity 2019;50:477–92.
36. Perez-Ruiz E, Minute L, Otano I, Alvarez M, Ochoa MC, Belsue V, et al. Prophylactic TNF blockade uncouples efficacy and toxicity in dual CTLA-4 and PD-1 immunotherapy. Nature 2019;569:428–32.
37. Im SJ, Hashimoto M, Gerner MY, Lee J, Kissick HT, Burger MC, et al. Defining CD8+ T cells that provide the proliferative burst after PD-1 therapy. Nature 2016;537:417–21.
38. Kurtulus S, Madi A, Escobar G, Klapholz M, Nyman J, Christian E, et al. Checkpoint blockade immunotherapy induces dynamic changes in PD-1^-CD8^+ tumor-infiltrating T cells. Immunity 2019;50:181–94.
39. Siddiqui I, Schaeuble K, Chennupati V, Fuertes Marraco SA, Calderon-Copete S, Pais Ferreira D, et al. Intratumoral Tcf1^+PD-1^+CD8^+ T cells with stem-like properties promote tumor control in response to vaccination and checkpoint blockade immunotherapy. Immunity 2019;50:195–211.
40. Jansen CS, Prokhnevska N, Master VA, Sanda MG, Carlisle JW, Bilen MA, et al. An intra-tumoral niche maintains and differentiates stem-like CD8 T cells. Nature 2019;576:465–70.
41. Horton BL, Williams JB, Cabanov A, Spranger S, Gajewski TF. Intratumoral CD8+ T-cell apoptosis is a major component of T-cell dysfunction and impedes antitumor immunity. Cancer Immunol Res 2018;6:14–24.
42. Zhu J, Powis de Tenbossche CG, Cané S, Colau D, van Baren N, Lurquin C, et al. Resistance to cancer immunotherapy mediated by apoptosis of tumor-infiltrating lymphocytes. Nat Commun 2017;8: 1404.
43. Villarroel-Espindola F, Yu X, Datar I, Mani N, Sanmamed M, Velcheti V, et al. Spatially resolved and quantitative analysis of VISTA/PD-1H as a novel immunotherapy target in human non-small cell lung cancer. Clin Cancer Res 2018;24:1562–73.
44. Finck R, Simonds EF, Jager A, Krishnaswamy S, Sachs K, Fantl W, et al. Normalization of mass cytometry data with bead standards. Cytometry A 2013;83:483–94.
45. Amir EAD, Davis KL, Tadmor MD, Simonds EF, Levine JH, Bendall SC, et al. ViSNE enables visualization of high dimensional single-cell data and reveals phenotypic heterogeneity of leukemia. Nat Biotechnol 2013;31:545–52.
46. Kim D, Langmead B, Salzberg SL. HISAT: a fast spliced aligner with low memory requirements. Nat Methods 2015;12:357–60.
47. Pertea M, Pertea GM, Antonescu CM, Chang TC, Mendell JT, Salzberg SL. StringTie enables improved reconstruction of a transcriptome from RNA-seq reads. Nat Biotechnol 2015;33:290–5.
48. Love MI, Huber W, Anders S. Moderated estimation of fold change and dispersion for RNA-seq data with DESeq2. Genome Biol 2014;15:1–21.

Published OnlineFirst March 3, 2021; DOI: 10.1158/2159-8290.CD-20-0962

CANCER DISCOVERY

AACR American Association for Cancer Research

A Burned-Out CD8$^+$ T-cell Subset Expands in the Tumor Microenvironment and Curbs Cancer Immunotherapy

Miguel F. Sanmamed, Xinxin Nie, Shruti S. Desai, et al.

Cancer Discov 2021;11:1700-1715. Published OnlineFirst March 3, 2021.

Updated version	Access the most recent version of this article at: doi:10.1158/2159-8290.CD-20-0962
Supplementary Material	Access the most recent supplemental material at: http://cancerdiscovery.aacrjournals.org/content/suppl/2021/03/04/2159-8290.CD-20-0962.DC1

Cited articles	This article cites 48 articles, 8 of which you can access for free at: http://cancerdiscovery.aacrjournals.org/content/11/7/1700.full#ref-list-1
Citing articles	This article has been cited by 1 HighWire-hosted articles. Access the articles at: http://cancerdiscovery.aacrjournals.org/content/11/7/1700.full#related-urls

E-mail alerts	Sign up to receive free email-alerts related to this article or journal.
Reprints and Subscriptions	To order reprints of this article or to subscribe to the journal, contact the AACR Publications Department at pubs@aacr.org.
Permissions	To request permission to re-use all or part of this article, use this link http://cancerdiscovery.aacrjournals.org/content/11/7/1700. Click on "Request Permissions" which will take you to the Copyright Clearance Center's (CCC) Rightslink site.

Downloaded from cancerdiscovery.aacrjournals.org on September 9, 2021. © 2021 American Association for Cancer Research.